Colloids and Surfaces A: Physicochemical and Engineering Aspects 648 (2022) 129213

Contents lists available at ScienceDirect

Colloids and Surfaces A: Physicochemical and Engineering Aspects

journal homepage: www.elsevier.com/locate/colsurfa

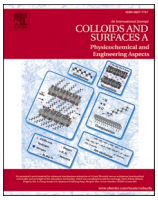

A criterion for when an emulsion drop undergoing turbulent deformation has reached a critically deformed state

Andreas Håkansson [a,*], Marco Crialesi-Esposito [b], Lars Nilsson [a], Luca Brandt [b,c]

[a] Department of Food Technology, Engineering and Nutrition, Lund University, SE-221 00 Lund, Sweden
[b] FLOW, Department of Engineering Mechanics, Royal Institute of Technology (KTH), SE-100 44 Stockholm, Sweden
[c] Department of Energy and Process Engineering, Norwegian University of Science and Technology (NTNU), NO-7491 Trondheim, Norway

GRAPHICAL ABSTRACT

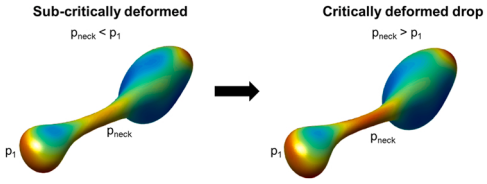

ARTICLE INFO

Keywords:
Emulsification
Drop breakup
DNS
Turbulence
Deformation
Emulsion

ABSTRACT

Turbulent breakup in emulsification devices is a dynamic process. Small viscous drops undergo a sequence of oscillations before entering the monotonic deformation phase leading to breakup. The turbulence-interface interactions prior to reaching critical deformation are therefore essential for understanding and modeling breakup. This contribution uses numerical experiments to characterize the critically deformed state (defined as a state from which breakup will follow deterministically, even if no further external stresses would act on the drop). Critical deformation does not coincide with a threshold maximum surface area, as previously suggested. A drop is critically deformed when a neck has formed locally with a curvature such that the Laplace pressure exceeds that of the smallest of the bulbs connected by the neck. This corresponds to a destabilizing internal flow, further thinning the neck. Assuming that the deformation leads to two spherical bulbs linked by a cylindrical neck, the critical deformation is achieved when the neck diameter becomes smaller than the radius of the smallest bulb. The role of emulsifiers is also discussed.

1. Introduction

Emulsion formation is important for many branches of chemical engineering processing, including the food and pharmaceutical industries [1–3]. Due to the high energy cost involved, there is a substantial industrial interest in improving design and operation of emulsification devices. Moreover, from a product formulation and process design perspective, there is a large interest in predictively modeling the emulsion drop size distributions form design and operating conditions [4,5].

Whether considering high-pressure homogenizers or rotor-stator mixers (the two major alternatives for industrial emulsification), drop breakup is mainly due to interactions with the turbulent flow structures [6–11].

Due to its large industrial relevance, turbulent emulsification has therefore been extensively studied, at least since the 1940 s. The Kolmogorov-Hinze framework [12–14] predicts that the largest drop

* Corresponding author.
E-mail address: andreas.hakansson@food.lth.se (A. Håkansson).

https://doi.org/10.1016/j.colsurfa.2022.129213
Received 30 March 2022; Received in revised form 2 May 2022; Accepted 10 May 2022
Available online 13 May 2022

Nomenclature

Abbreviations

DNS	Direct numerical simulation
MTHINC	Multi-dimensional tangent hyperbola interface capturing (algorithm)
PBE	Population balance equation.
VOF	Volume-of-fluid

Symbols (Latin)

A	Interfacial area of drop, m^2
a, b, c	Half-axes of ellipsoidal drop, m
A_0	Initial interfacial area of (spherical) drop, m^2
D_0	Initial diameter of (spherical) drop, m
D_{neck}	Diameter of neck at critical state, m
H	Gaussian curvature, m^{-2}
K	Mean curvature, m^{-1}
K_{min}	Average of the 10% lowest values of K on the interface, m^{-2}
L, B	Length (breadth) of ellipsoidal drop, m
p	Static pressure, Pa
p_0	Static pressure outside of drop interface, Pa
p_1, p_2	Static pressure in the smallest (largest) drop bulb, Pa
p_{neck}	Pressure in the neck, Pa
p_{sph}	Laplace pressure of a sphere with diameter D_0, Pa
p_{tip}	Static pressure at tip of the ellipsoidal drop, Pa
p_{waist}	Static pressure at waist of the ellipsoidal drop, Pa
r	Length-to-breadth ratio of ellipsoidal drop, -
R	Radius, m
R_0	Initial radius of (spherical) drop, m
R_1, R_2	Radii of smallest (largest) drop bulb at critical state, m
t	Time from injecting drop into turbulence, s
t_B	Time of initial breakup, s
t_C	Time when reaching the critically deformed state, s
v	Velocity in y-dimension, $m\ s^{-1}$
We	Weber number, -
x, y, z	Spatial dimensions, m

Symbols (Greek)

γ	Interfacial tension, $N\ m^{-1}$
ε	Dissipation rate of turbulent kinetic energy, $m^2\ s^{-3}$
θ	Polar angle, rad
κ_1, κ_2	Principal curvatures, m^{-1}
ρ_C	Continuous phase density, $kg\ m^{-3}$
τ_{ads}	Characteristic time of emulsifier adsorption, s
τ_{def}	Characteristic time of drop deformation, s
τ_{spr}	Characteristic time of emulsifier surface spreading, s
τ_η	Kolmogorov time-scale, s
υ_C	Kinematic viscosity of continuous phase, $m^2\ s^{-1}$
φ	Azimuthal angle., rad

diameter surviving prolonged exposure to a turbulent field is given by a balance between the stabilizing Laplace pressure and the disrupting turbulent stresses, arising from the combination of pressure fluctuations from small turbulent structures (turbulent inertial breakup) and viscous shear from larger turbulent structures (turbulent viscous breakup). This framework has later been extended to include the additional stabilization arising from drop viscosity [15–17], and the effect of the intermittent nature of the turbulent flow [18,19]. The extended Kolmogorov-Hinze framework performs well in terms of predicting the largest surviving drop diameters across a wide variety of conditions [20].

During the last decades, substantial advances have also been made in terms of theoretically constructing and experimentally measuring turbulent fragmentation rates in emulsification devices, allowing for the prediction of how the entire drop size distribution evolves during turbulent emulsification using a population balance-equation (PBE) framework [21–26].

Aiming to build a fundamental understanding of how drop interface and turbulence interacts during the emulsification process, and to improve the prediction based on the previously mentioned modeling approaches, there is a great need for detailed experimental investigations of the breakup process. An increasing number of high-quality single-drop breakup investigations have been presented during the last couple of years. This includes both in vitro experimental high-speed breakup visualizations [9,27–33] and *in silico* numerical experiments using model-free direct numerical simulation (DNS) with highly resolved interface tracking [34–40]. Comprehensive reviews can be found elsewhere [41,42].

Much is still unknown or debated when it comes to the details of how turbulent structures give rise to critical deformation and breakup in emulsification devices; for example, if drops are typically deformed or 'primed' by the laminar flow upstream of the turbulent zone [9,10] or enter the turbulent zone in a spherical state [8], if drop breakup is due to short-ranged 'collisions' between turbulent eddies [43,44] or longed-ranged interactions [45]. There is also an ongoing debate whether drops are critically deformed by single turbulent eddies [35,46] or a larger collection thereof [31,34], and on how drops and critically deforming vortex/vortices are oriented with respect to each other during the critical stage [40,45,46].

Nevertheless, it is clear that drop breakup is a dynamic process characterized be several separate stages. From an application perspective, the behavior of the drops just large enough to break is of special importance (since these set the limit for physical stability of the product and energy efficiency of the device). When these relatively small drops enter a turbulent flow, they are often seen to first go through a sequence of deformation followed by subsequent relaxation back to a nearly spherical state [27,34,36]. Provided the interaction time is sufficient, this oscillation phase may end and the drop may deform to the degree that the first fragment detaches. This is referred to as the state (or time) of 'initial breakup' [32]. The fragments are, however, often deformed and, thus, continue breaking.

Xing et al. [44] further divided the deformation phase, from relaxed state to initial breakup, into two parts: a deformation sub-phase where the surrounding turbulence interacts with and deforms the drop until it has reached a critically deformed state, and a relaxation sub-phase mainly controlled by the internal flow resulting from the deformed state.

Ashar et al. [6], following the same line of thought, suggested that in-depth analysis of the time and position at which the drop has just been critically deformed is needed to understand what separate conditions leading to drop breakup from those that do not, and hence, that this position/time is of large importance for optimizing the geometrical design of an industrial machine.

Formally, we define the state of critical deformation as when the drop has been irreversibly deformed to such an extent that it will eventually (and deterministically) break even if the turbulent interactions were to cease instantly (i.e., even without any further external stress acting on the drop). From an experimental perspective, however, it is difficult to determine where in a sequence of high-speed visualization frames this condition is met. Qi et al. [31] recently focused their attention on the turbulent interactions up to 6 ms prior to the initial breakup in an attempt to describe this critical phase. Ashar et al. [6] and later Karimi and Andersson [35] suggested that the critically deformed state is attained when the drop interface area reaches its maximum value (prior to breakup). The drop interface area is directly proportional to the

surface energy (assuming a constant interfacial tension), and in fragmentation rate models [23,26], it is often assumed that breakup occurs (deterministically) once the turbulent vortices have transferred an amount of energy to the drop corresponding to the increase in interfacial energy resulting from a breakup event. This notion was further refined by Andersson and Helmi [46] showing that the interfacial energy of a deforming drop must exceed the energy of the final state plus a 'transition state energy barrier'. However, the relationship between the evolution of interfacial energy and breakup is complex, as illustrated by Komrakova [36], showing that drops can relax from larger interfacial areas than those reached just prior to initial breakup.

Critical states or geometrical conditions, separating drop deformations leading to relaxation from those leading to detachment/breakup have also been investigated for other multiphase flows. Planchette et al. [47] pointed to the importance of taking into account more complex viscous and finite-size effects as well as capillary pressure in the identification of such a critical state for an asymmetrical liquid filament. Thus, it is far from obvious that the critically deformed state actually coincides with that of maximum interfacial area for turbulent emulsification, and further investigations are needed.

To the best of the authors' knowledge, there is of yet no generally accepted methodology for identifying the critically deformed state of a drop undergoing turbulent breakup. Moreover, such a criterion is in great need for identifying at what point (or range of points), in time and space, the drop undergoes the turbulence-interface interaction that controls breakup.

Ideally, one would want to extract drops at different states and instantly transfer each of them to a stagnant fluid to find the critically deformed state. This is not feasible in an in vitro experimental setting but possible to do in an *in silico* numerical experimental setting.

This contribution is part of a larger project aiming to increase the general understanding of turbulent drop breakup in industrially relevant emulsification devices, using a combination of numerical experiments and breakup visualizations. In a previous contribution [34], we developed a numerical experiment tool for studying the breakup of drops (in conditions similar to a high-pressure homogenizer) using DNS and highly resolved interface tracking, and started building a library of drop breakup sequences. It was concluded that breakup morphology differs greatly with the Weber number. However, no clear conclusions could be drawn on which turbulent structure is most influential for breaking the drop, partially due to a lack of understanding of when the drop has become critically deformed.

Here, we: (1) suggest a method based on numerical experiments to identify when a viscous drop undergoing turbulent breakup has reached a critically deformed state, (2) discuss what distinguishes this state from a sub-critical state and (3) suggest an objective criterion that can be used to identify the critically deformed state (i.e., in an experimental setting).

The investigations are limited to systems with large continuous to disperse phase density and viscosity (i.e., to emulsion drops as opposed to foam bubbles). Finally, note that the external stress deforming the drop up to the point of critical deformation is not analysed in detail in this contribution.

2. Materials and methods

2.1. Selection of cases and settings

A library of numerical drop breakup experiments in a periodic cube of isotropic and homogenous turbulence was created as a part of previous study [34]. Fig. 1 displays the morphology of 14 different drops at the point of initial breakup (Drop A-D are identical to those presented in Ref. [34] whereas the remaining drops have been generated by repeating the procedure described therein, see Table 1 for settings). For all cases, the Weber number,

Table 1
Parameters of the DNS used to generate the drop breakup library. Note, following conventions, the DNS setup is in dimensionless form.

Domain size	$(2\pi)^3$
Mesh size	128^3
Dissipation rate of turbulent kinetic energy, ε	3.1
Kolmogorov length-scale	0.092
Taylor length-scale	0.64
Kolmogorov time-scale	0.14
Taylor Reynolds number	33

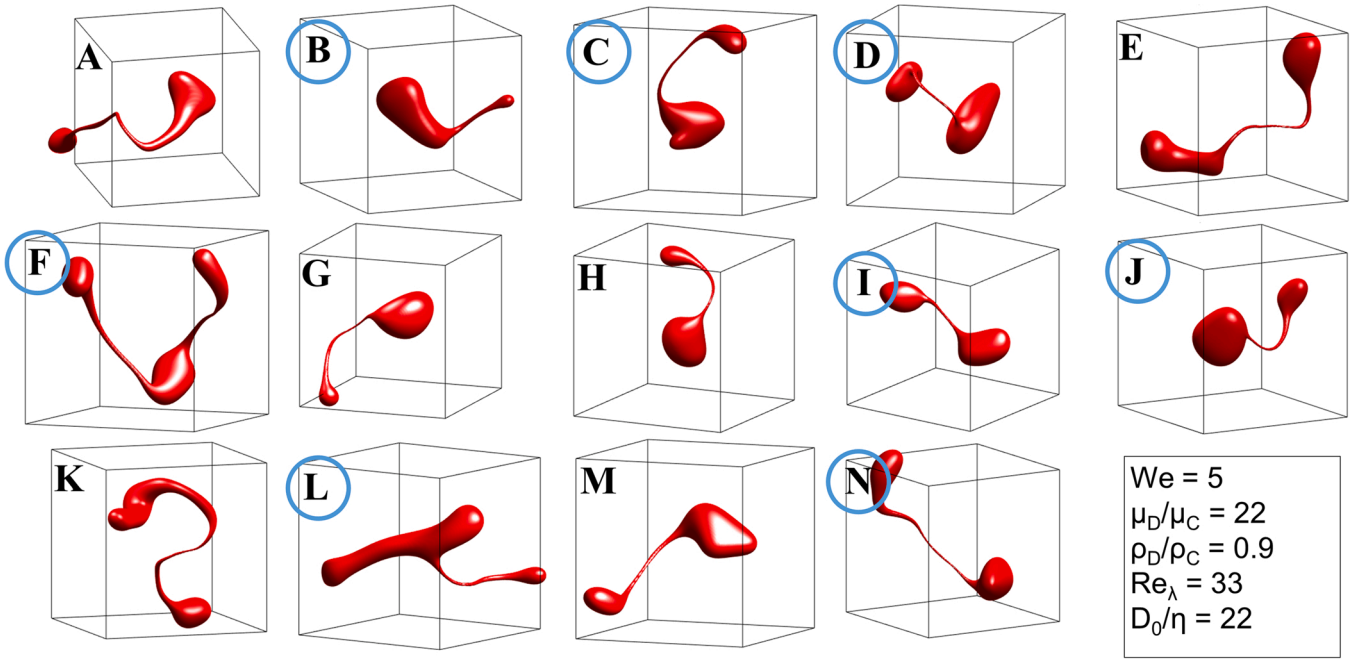

Fig. 1. Drop breakup library, showing the morphology of 14 drops at their state of initial breakup after being subjected to isotropic, homogenous turbulence. (Drops A-D are the same as used in the analysis in Ref. [34]). Blue rings indicate cases selected for detailed stability analysis in the present study.

$$We = \frac{2 \cdot \rho_C \cdot \varepsilon^{2/3} \cdot D_0^{5/3}}{\gamma} = 5, \quad (1)$$

where γ is interfacial tension (assumed constant over time and space), D_0 is the initial drop diameter, ρ_C is the continuous phase density and ε is the dissipation rate of turbulent kinetic energy obtained as the average across the computational cube and averaged across a 500 τ_η simulation time interval (sampled after the single-phase flow has converged but before drop injection). The Kolmogorov time-scale is defined as,

$$\tau_\eta = \sqrt{\frac{\upsilon_C}{\varepsilon}}. \quad (2)$$

All dimensionless numbers and turbulence characteristics reported are based on the one-phase ε.

The disperse to continuous phase density ratio is set to 0.9 and the disperse to continuous phase viscosity ratio is set to 22. The initial drop diameter, D_0, to Kolmogorov micro-scale is 22 and the Taylor-scale Reynolds number is 33. As argued in the previous study [34], these conditions correspond to the smaller (limiting) drops entering a high-pressure homogenizer (e.g., dairy processing), except that the Reynolds number is lower (to reduce computational cost).

Each of the 14 drops in Fig. 1 is the result of a separate flow realization. To create these, a single-phase forced isotropic and homogenous turbulence simulation is first set up in the domain and run until convergence. After convergence, 14 snapshots are collected at instants separated by no less than 100 τ_η. Each drop breakup realization is obtained by injecting a spherical drop into each of the 14 flow realizations. Under these conditions, all drops break before 65 τ_η. This configuration can be compared to that of a drop passing through the high-intensity turbulent zone of a high-pressure homogenizer valve, where hold-up is approximately 20–100 τ_η [34].

As seen in Fig. 1, most drops display a breakup morphology consisting of two bulbs separated by a thin filament for this Weber number. Nevertheless, some drops display a different behavior. Drop B shows a narrow tail-like structure having been pulled out of the drop at the initial breakup and drop L shows a thin thread extending out from a larger structure which is itself deformed. For drop K, the larger of the two bulbs is highly deformed at the state of initial breakup and for drop F, three bulbs with two interconnecting filaments characterize the morphology at the initial breakup.

Eight of these cases where analysed further in the present study: B, D, E, F, I, J and L. These cases were selected to include a substantial number of the most typical morphology and also more unusual shapes.

2.2. DNS methodology to identify the critically deformed state

The drop deformation library contains instantaneous velocity, pressure and interface location data (via the volume-of-fluid (VOF) field) across the computational domain, from injection to initial breakup, with a temporal resolution of $\approx 0.02\ \tau_\eta$ (the resolution varies due to using an adaptive time-stepping solver in the underlying DNS). Instants appearing to be close to the critical state are manually selected and analysed (see below). For each drop, this procedure is repeated so as to identify two time instants, one prior to the critical state (i.e., not breaking when transferred to quiescent conditions) and one after reaching the irreversible critically deformed state (i.e., breaking when transferred to quiescent conditions), separated by less than 1.3 τ_η.

To determine if a state is critically deformed or not, the DNS data (velocity, pressure and VOF) inside of the drop (defined as where VOF > 0.5) is transferred to a domain with quiescent flow (zero velocity and pressure). The intention is to, as closely as possible, replicate the thought-experiment of a drop being instantly transported from a turbulent flow to quiescent conditions. This also implies that a discontinuity in velocity and pressure will occur (as if one would be able to instantly transfer a drop to a quiescent fluid). However, this discontinuity will disappear rapidly as the simulation progresses (similarly to what happens after numerically injecting a new drop in any numerical breakup experiment).

The same DNS code that was used to generate the breakup sequence library (Fig. 1), is used without turbulent forcing to follow the droplet evolution when the turbulence is suddenly quenched. The numerical method, based on an in-house DNS with the multi-dimensional tangent hyperbola interface capturing method (MTHINC) [39,48], has been described and validated elsewhere [39,49,50]. The spatial resolution, corresponding to 0.5 Kolmogorov-microscales, ensures that the DNS is well-resolved [51]. This mesh corresponds to a resolution of 41 grid points across the initial drop diameter and 128 grid points across the periodic computational domain. Mesh resolution investigations show that differences are small compared to a case run with double resolution (i.e., the error in total interfacial area is less than 2%) [34]. The numerical mass-loss during the simulation is less than 0.002% for all investigated cases.

Fig. 2 displays an example of such a stability analysis (drop E). The upper row shows how the drop at $t/\tau_\eta = 48.1$ evolves when transferred to a quiescent fluid. As seen in the figure, the drop relaxes and returns to a spherical state after approximately 4.5 τ_η. Thus the drop to the far left in the upper row is in a pre-critical state. The second row displays how the same drop evolves when transferred from a somewhat later state ($t/\tau_\eta = 49.3$). As seen in the sequence, the drop now continues to deform despite not being exposed to external stress and breaks up after 3.3 τ_η. Thus, the drop to the far left of the lower row is in a critically deformed state. Consequently, for drop E, the critically deformed state is reached somewhere in the interval (48.1–49.3] τ_η. Note that the morphological differences between the pre-critical and critical states are small, thus the method allows for making relatively fine distinctions between what separates critical from pre-critical conditions. Also note that the breakup sequence in Fig. 2 should only be used as a tool for identifying a critical state. It is not representative of turbulent drop breakup, since the continuing presence of turbulence-interface interactions determines the actual morphology at the initial breakup (cf. [44]). This can also be seen by comparing the state of breakup under quiescent conditions (Fig. 2, lower right panel) to the state of drop E when it reaches initial breakup in the turbulent flow (see Fig. 1E).

2.3. Properties of the drop interface

The total drop interface area at each time is calculated by numerically integrating the VOF gradient, with an adaptive quadrature algorithm [52], used as implemented in the 'integral'-function in MATLAB 2019a (MathWorks, Natick, MA). The local curvature of the drop surface from injection to initial breakup is calculated using a discrete explicit-point cloud-based algorithm [53], used as implemented in ParaView 5.7.0 [54]. The algorithm allows for the calculation of Gaussian curvature, K, and mean curvature, H, for each point on the drop surface. These are related to the two principal curvatures (defined as the inverse of the two radii of curvature), κ_1 and κ_2, by

$$H = (\kappa_1 + \kappa_2)/2, \quad (3)$$

$$K = \kappa_1 \cdot \kappa_2. \quad (4)$$

The principal curvatures are calculated from [55],

$$\kappa_1 = H + \sqrt{H^2 - K}, \quad (5)$$

$$\kappa_2 = H - \sqrt{H^2 - K}. \quad (6)$$

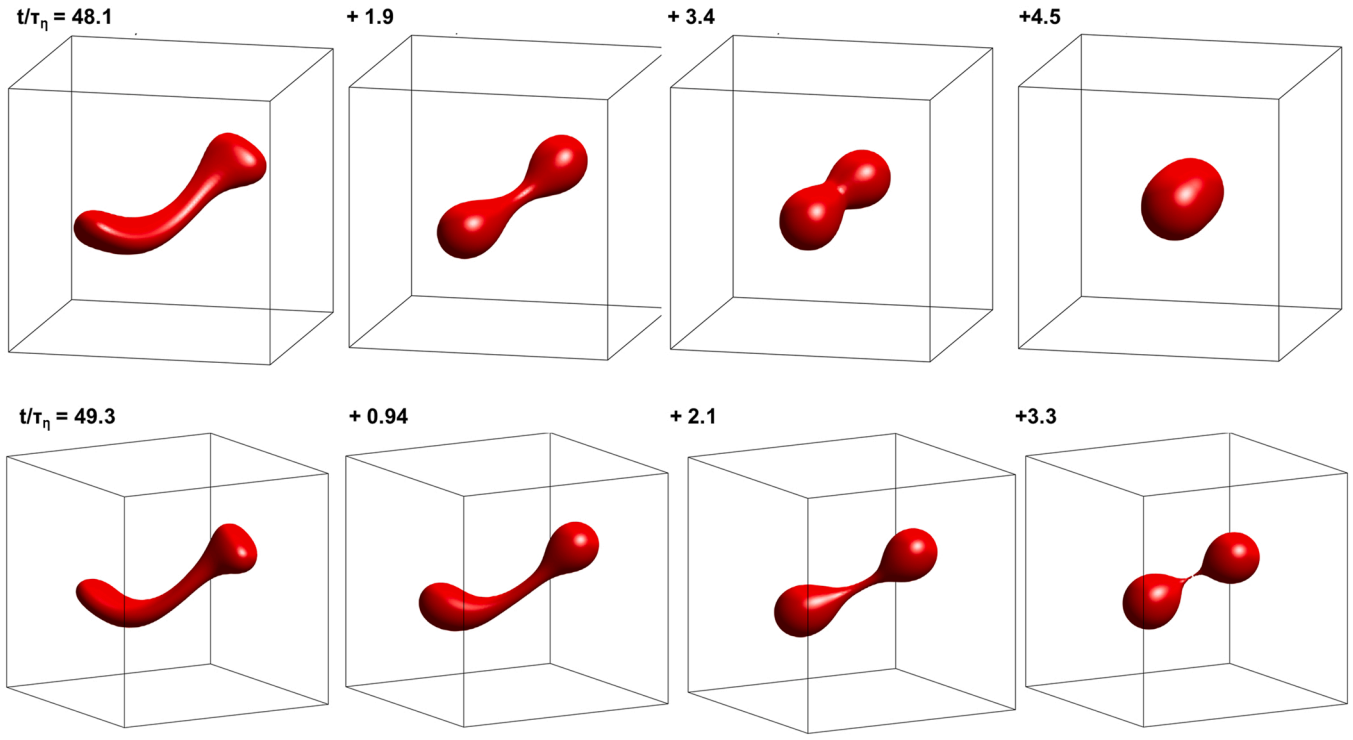

Fig. 2. Identification of critical state. Upper row: Showing how drop E, at the deformation reached after $t/\tau_\eta = 48.1$, relaxes to a sphere after being transferred to a quiescent fluid. Lower row: showing how the same drop, at the deformation reached at $t/\tau_\eta = 49.3$, breaks if placed in a quiescent fluid.

2.4. Ellipsoidal deformation – an ideal case

As a contrasting ideal case, it will prove informative to consider a pure ellipsoidal deformation, i.e., a spherical drop deforming in such a way so it remains a prolate spheroid throughout the process (semiaxes $a = B/2$, $b = B/2$, $c = L/2$), but with an increasing length-to-width ratio $r = L/B$. Denoting the initial (undeformed) drop diameter by D_0, volume conservation implies that the axes of the ellipsoid can be expressed as a function of D_0 and the deformation ratio, r:

$$B = r^{-1/3} \cdot D_0, \tag{7}$$

$$L = r^{2/3} \cdot D_0. \tag{8}$$

For an ellipsoid, the Gaussian and average curvature on the surface can be analytically calculated [56] as:

$$K = \frac{(abc)^2}{\left[a^2b^2\cos^2(\theta) + c^2\sin^2(\theta)\left(b^2\cos^2(\phi) + a^2\sin^2(\phi)\right)\right]^2}, \tag{9}$$

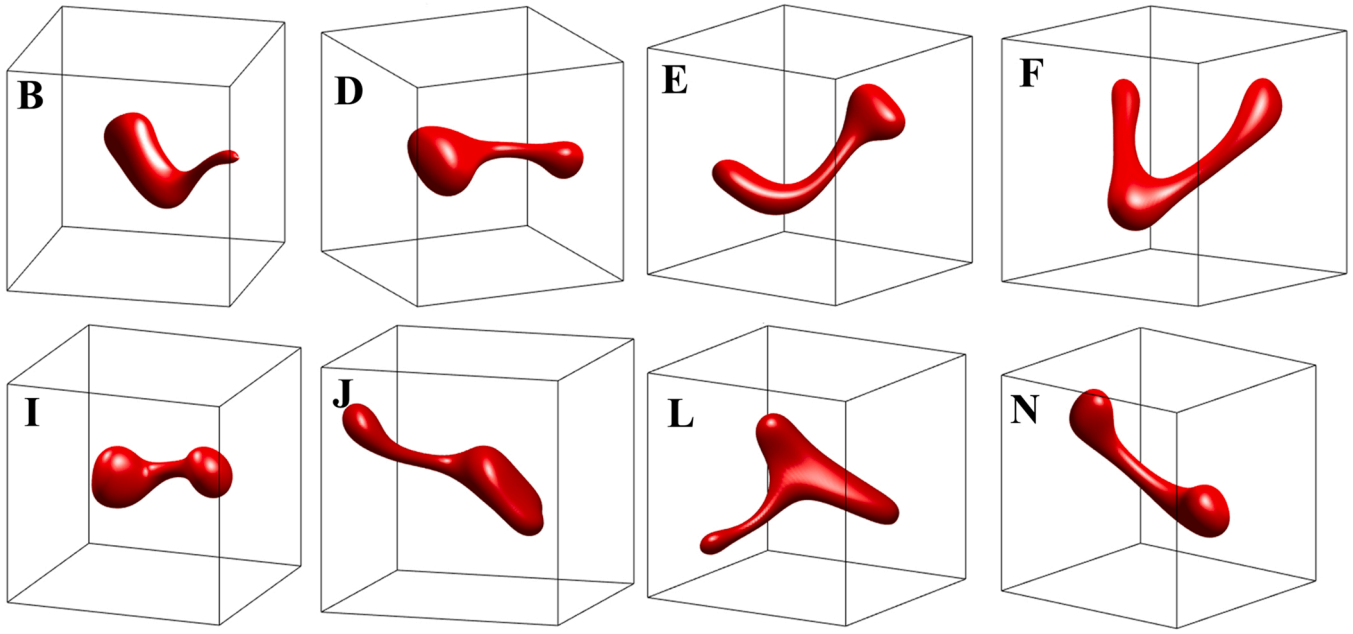

Fig. 3. Drop morphology at the critically deformed state.

$$H = \frac{abc\left[3\left(a^2+b^2\right)+2c^2+\left(a^2+b^2-2c^2\right)\cos\left(2\theta\right)-2\left(a^2-b^2\right)\cos\left(2\phi\right)\sin^2(\theta)\right]}{8\left[a^2b^2\cos^2(\theta)+c^2\sin^2(\theta)\left(b^2\cos^2(\phi)+a^2\sin^2(\phi)\right)\right]^{3/2}}, \quad (10)$$

where $0 \leq \theta < \pi$ and $0 \leq \varphi < 2\pi$ are the polar and azimuthal angles in a spherical coordinate system. The principal curvatures are then calculated using Eqs. (5) and (6).

3. Results and discussion

3.1. Morphology at critical deformation

Fig. 3 displays all eight drops at the critically deformed state (i.e., at the first instant for which the drop will break if instantly transferred to quiescent conditions). First note that for all investigated cases, the critical state is characterized by the formation of a neck. Comparing the morphology at the critically deformed state (Fig. 3) to that at initial breakup (Fig. 1) reveals that the neck develops into the thin filament where the first detachment takes place. However, comparing the different drops, large variations in the dimension of the neck at the critically deformed state are also evident. For drop I, the neck has become critical already at a neck diameter of 0.5 R_0 whereas for drop B, the critical state is not reached until the neck has been reduced below a diameter of 0.17 R_0. Thus, the neck diameter is, in itself, not a viable criterion for identifying the critical state.

For a majority of the cases (I, D, E, J and N) the neck extends between two more or less clearly defined bulbs. Comparing to the morphology at critical breakup shows that these are the cases where initial breakup results in two larger fragment and an array of filament satellites. For drops B and L, however, the neck appears to form from the pulling out of smaller thread-like structures from the drop. For drop F, instead, the deformation results in three smaller bulbs (connected by two different necks). Also in this case, this difference remains until reaching the state of initial breakup.

The time between when a drop is injected into the turbulence and when it reaches the critical state differs between drops (7.0–59 τ_η). This can be attributed to the fact that the deformation is non-monotonic for most cases, with drops going through a stochastic number of deformation-relaxation cycles (or 'oscillations') before starting the deformation that will eventually give rise to the critical state [27,34,36]. The time between the critical state and the initial breakup (t_B - t_C) is a more interesting characteristic of the breakup process, related to the second sub-phase according to the definition in Xing et al. [44]. This time-scale also differs between cases. However, it is somewhat correlated (Pearson correlation of +0.66) to the neck diameter at the critical state (see Fig. 4). For drop B (with the thinnest critical neck), breakup occurs already 4 τ_η after the critical state, whereas for drop I (thickest critical neck), breakup requires 11 τ_η after the critical deformation has been reached, reflecting the fact that initial breakup occurs with a more uniform neck diameter than the critical state.

3.2. Interfacial energy and the critically deformed state

Fig. 5 displays the evolution of the interfacial area (normalized to its initial value), A/A_0, for the eight drops, from injection into the turbulence ($t = 0$), until the initial breakup (endpoints of the different curves in Fig. 5). The critically deformed state (Fig. 4) is marked with a diamond marker. The interfacial area at the critically deformed state differs between drops (A/A_0 =1.30–1.65), with an average of 1.44. The interval is narrower than that pertaining the state of initial breakup (A/A_0 = 1.32–1.81).

As mentioned above, the critical state has previously been assumed to occur once the drop interfacial area has reached its maximum value prior to breakup. The results in Fig. 5 show that this is not typically the case. For four drops (B, E F and N), the critically deformed state occurs before the last local maxima of A/A_0. For two drops (I and J), the critically deformed state is found later than that of maximum surface area and for one drop (L), the surface area increases monotonically over time from injection to breakup. Only one drop (D) obtains its critically deformed state close to where the surface area is maximal (i.e., within 1.2 τ_η from it).

In summary, the critically deformed state cannot be identified as the time when the surface area has reached its maximum value.

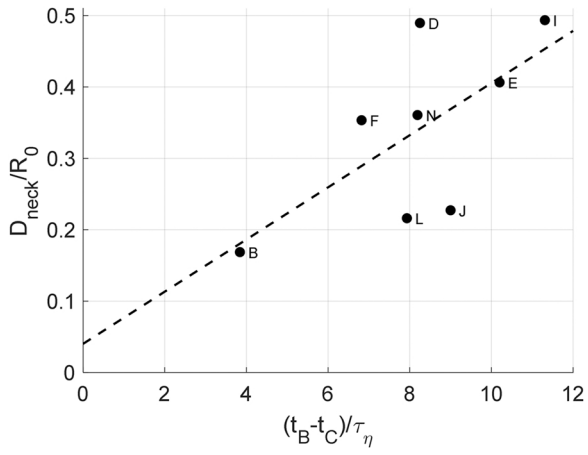

Fig. 4. Correlation between neck diameter at the critically deformed state (D_{neck}) and the time between reaching the critical state and initial breakup (t_B-t_C). Markers show results from numerical experiments, line is a linear regression.

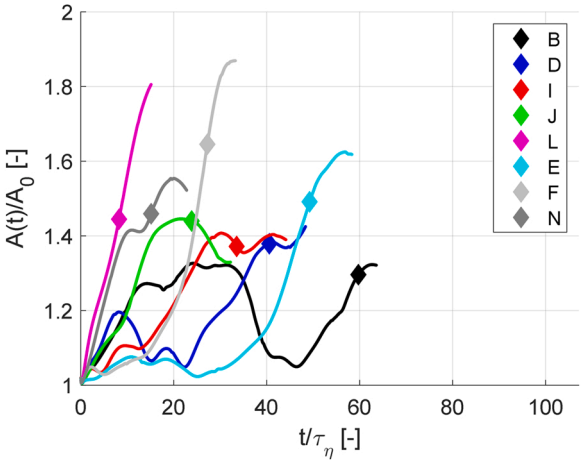

Fig. 5. Evolution of normalized drop interface area, A/A_0, as a function of normalized time, $t/\tau_{\eta 0}$, for the eight drops under consideration. Diamond markers show the time of the critical deformation whereas the endpoint represents the point of initial breakup.

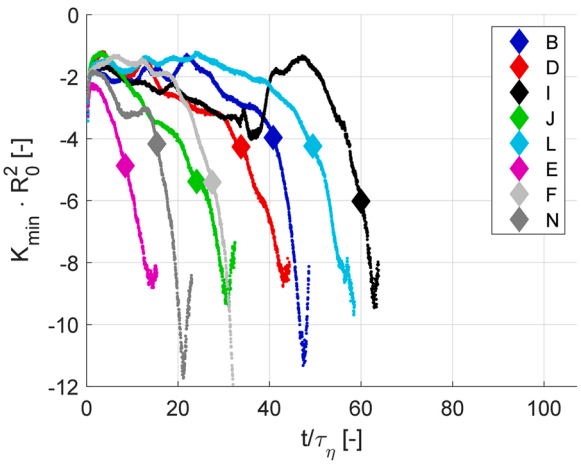

Fig. 6. Evolution of minimal normalized Gaussian curvature, $K_{min} \cdot R_0^2$, as a function of normalized time, t/τ_η, for the eight drops under consideration. Diamond markers show the time at critical deformation whereas the endpoint represents the point of initial breakup.

3.3. Local curvature and the critically deformed state

Fig. 3 suggested that the formation of a neck is essential for the occurrence of the critical state. Geometrically, a neck can be characterized by bands of saddle points across its waist and saddle points are characterized by a negative Gaussian curvature. Fig. 6 displays the Gaussian curvature of the most pronounced saddle points on the drop interface as a function of time, comparing the eight drops under investigation (i.e., K_{min} is defined as the average of the 10% of the surface points with lowest Gaussian curvature).

Fig. 6 illustrates how the Gaussian curvature does start to decrease substantially in the sequence leading up to the critical state. At the critical state, $K_{min} \cdot R_0^2$ ranges from − 6.0 to − 4.0. Thus, it is not possible to find a precise K_{min} that identifies the critical state. However, K_{min} is a better indicator for critical deformation than A/A_0. Looking at drop B (an outlier when attempting to use A/A_0 to identify the critically deformed state), the neck is substantially more curved at the critical state than at the state the drop relaxed from (as opposed to interfacial area, see Fig. 5). Moreover, the state that B is able to relax from ($K_{min} = -3.9$ at $t/\tau_\eta = 36$) is also (slightly) less curved than that giving rise to breakup for the other drops.

In summary, the curvature analysis supports the idea of taking the local deformation of the neck into account when characterizing the critically deformed state. However, curvature still fails to provide a clear criterion for the occurrence of a critical state.

3.4. Static pressure distribution at the critically deformed state

The critical state is defined as leading to a continued deformation even when removing all external stress. This suggests that the critically deformed state has an internal flow that is destabilizing (as opposed to a sub-critical state, where the internal flow is stabilizing the drop, leading to contraction and relaxation when removing external stresses). In an attempt to illustrate the force driving this internal flow, the upper row in Fig. 7 displays the static pressure distribution in a plane cutting through drop D at three time instances: two instances prior to reaching the critically deformed state (a: $t/\tau_\eta = 38.5$ and b: $t/\tau_\eta = 40.1$), and one just after the critically deformed state has been reached (c: $t/\tau_\eta = 41.0$). The lower row show 3D representations (isosurfaces of VOF = 0.5), colored by surface pressure, together with the location of the planes seen in the upper row (the pressure is normalized with p_{sph}, the Laplace pressure for a sphere with diameter D_0). Note that the planes cut through the two bulbs and the interconnecting neck. Starting with the first instant (a), three regions with high local static pressure can be identified inside the drop: one in each bulb and one in the neck. The global pressure maximum is located in the smaller (lower) bulb, resulting in a net flow of

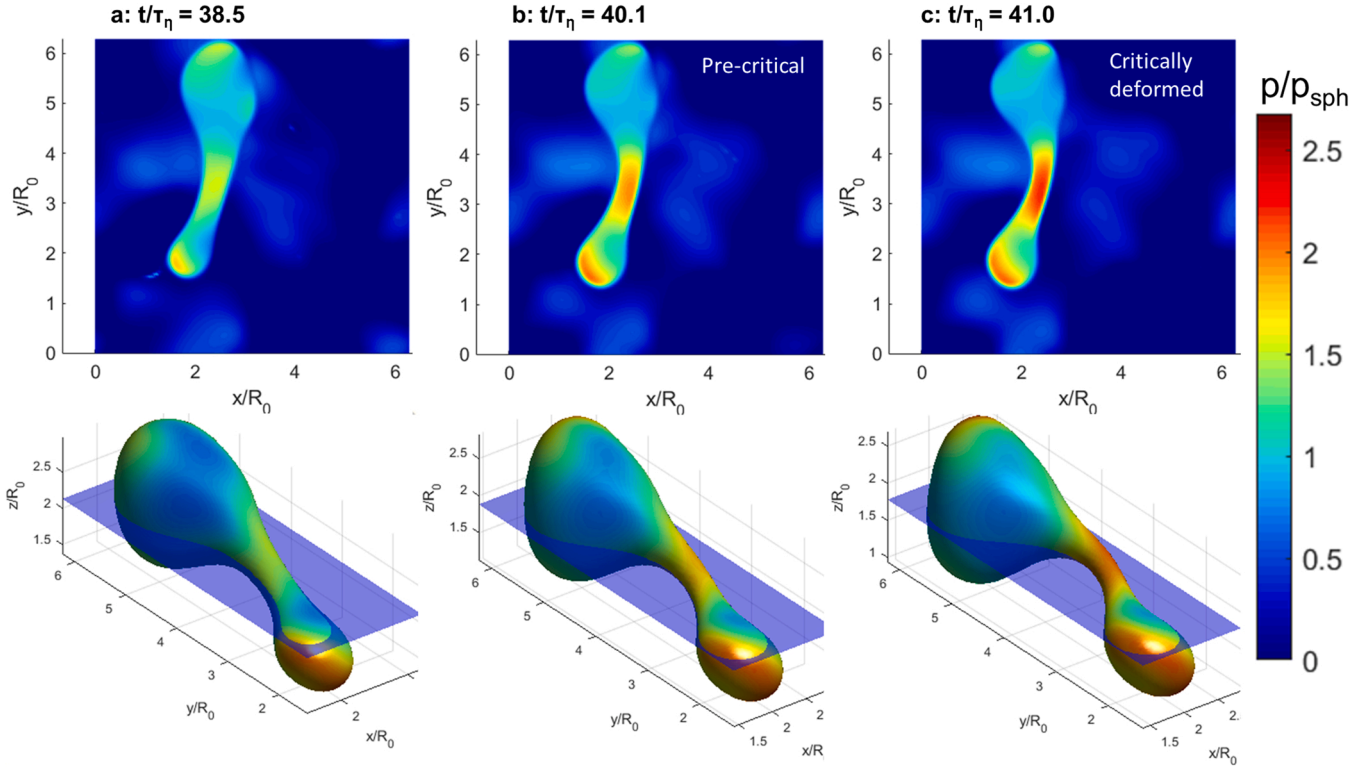

Fig. 7. Static pressure distribution in a plane cutting through the center of drop D (upper row) and surface pressure, p, normalized to the Laplace pressure of a sphere, p_{sph} (second row) at three instances: a: $t/\tau_\eta = 38.5$, b: $t/\tau_\eta = 40.1$, and c: $t/\tau_\eta = 41.0$, the last of which (c) corresponds to the critically deformed state.

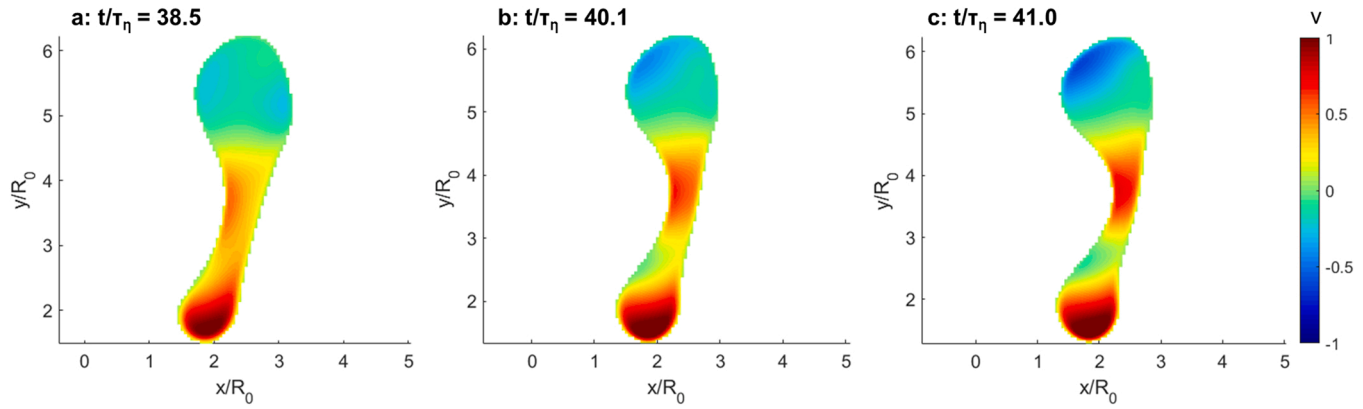

Fig. 8. Contours of upward (y-direction) velocity, v, inside the drop, at the same three instances and planes as in Fig. 7. (Drop D).

liquid in the upward direction (i.e., a positive v in Fig. 7a). This explains why the drop is not critically deformed. The internal flow is stabilizing, pushing fluid back to the largest bulb.

As time progresses (Fig. 8b-c), the pressure in the neck increases. Just before the critically deformed state (b: $t/\tau_\eta = 40.1$), the neck pressure has almost reached the value of the lower bulb. At the critically deformed state (c: $t/\tau_\eta = 41.0$), the pressure inside the neck exceeds that of the smaller (lower) bulb for the first time. This explains why the drop is critically deformed: since the flow follows the direction of negative pressure gradient, the fluid in the lower part of the neck will start flowing back to the smaller bulb whereas the fluid in the upper part of the neck continues to flow into the upper bulb (see Fig. 8c). This results in a depletion of fluid in the neck, until rupture. Thus, the internal flow is destabilizing.

Figs. 3 and 6 suggest that local neck curvature determines whether this critical deformation has been reached. We recall that the Young-Laplace equation describes the relationship between interfacial curvature and internal pressure: the pressure difference across the interface at a location with principal curvatures κ_1 and κ_2 is:

$$\Delta p = \gamma(\kappa_1 + \kappa_2). \tag{11}$$

We use the Young-Laplace equation to explain the observation in Figs. 7 and 8. First note that the pressure is inversely proportional to the radius R of a spherical droplet, reducing Eq. (11) to

$$\Delta p = \frac{2\gamma}{R}. \tag{12}$$

Consequently, the smaller of the two bulbs will display the highest static pressure (Fig. 8a-b) and the net flow will be from the smaller to the larger bulb (in the pre-critical state) (Fig. 8a-b). When the drop is deformed, with external turbulent stresses leading to a thinning of the neck, the local curvature increases. As the curvature increases, so does

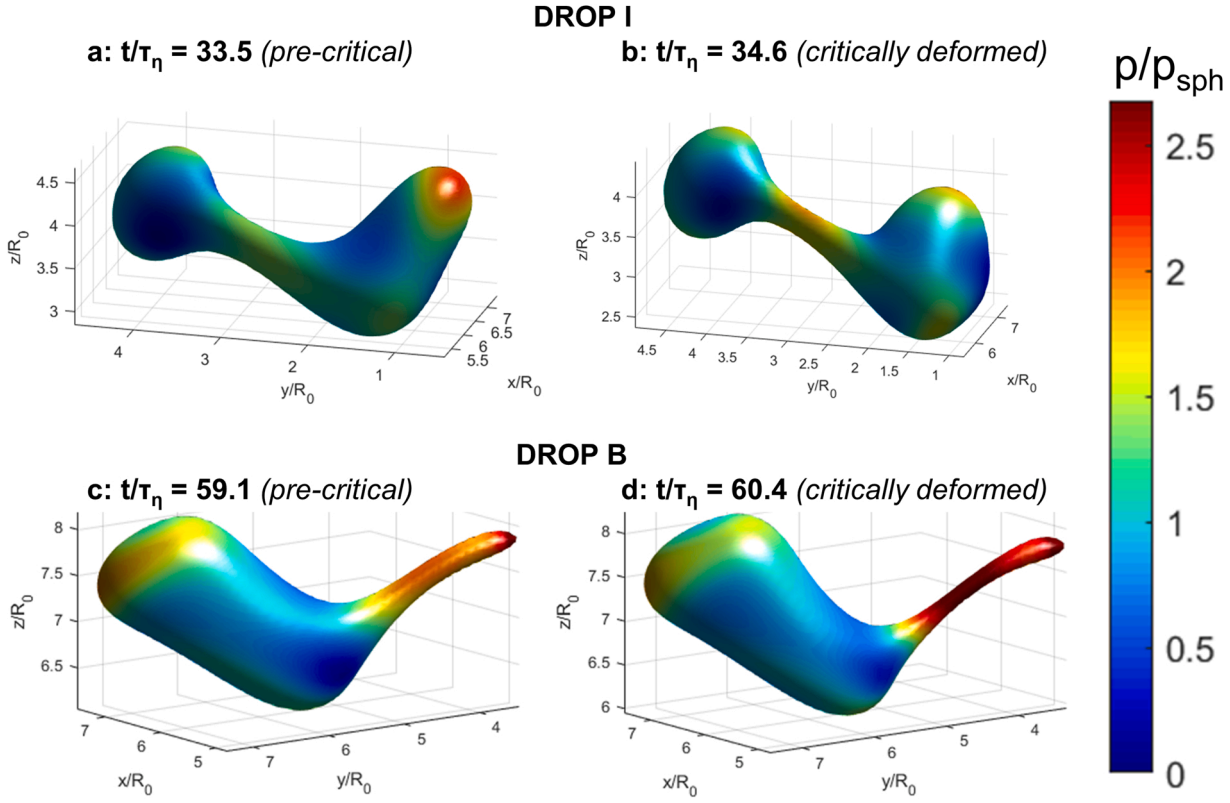

Fig. 9. Surface pressure, p, of pre-critical states (a and c) and critically deformed states (b and d), comparing the drop with the largest critical neck diameter (drop I, frames a-b) to the drop with the smallest critical neck diameter (drop B, frames c-d).

the static pressure in the neck (Eq. (11)). At the critical state, the neck curvature is, for the first time, sufficiently large to exceed that of the smallest bulb. Once the drop has been deformed enough to reach such a high neck curvature, the internal pressure gradient is reversed and internal flow will deplete the neck. This will further increase the neck curvature resulting in a larger pressure gradient, accelerating the process.

To confirm this hypothesis, Fig. 9 displays a similar comparison for two other drops (drops I and B), comparing the surface pressure in a pre-critical state (left) to the critically deformed state (right). Drops I and B differ greatly in the breakup morphology (see Figs. 1 and 3). Drop I deforms into two approximately equally sized bulbs separated by a neck that is comparably thick at the critical state, whereas drop B has the smallest neck dimension at critical conditions of the studied cases (see Fig. 4). However, for both cases, the same criterion appears to control the transition from a pre-critical to a critical deformation: the drop is critically deformed as soon as the neck is sufficiently thin to create a higher static pressure in the neck than in the smallest bulb. We never observe a situation, fulfilling these conditions, from which the drop is able to relax. Moreover, this also explains why the neck diameter needs to be substantially smaller for drop B than for drop I before reaching the critical state (see the ordinate scale in Fig. 4). The smaller the smallest of the two bulbs is, the higher is the Laplace pressure in this bulb, and the more deformed the neck needs to be before the neck pressure exceeds that of the smallest bulb. (See Section 3.6 for an attempt to extend this observation into a geometric criterion, easier to use under experimental conditions.).

3.5. The ideal case of ellipsoidal deformation

To further illustrate the importance of a curved neck for this critical state to emerge, a comparison to the case of ideal ellipsoidal deformation will prove informative. Consider a sphere (with initial diameter D_0), deforming in such a way so it remains a prolate ellipsoid with increasing length-to-width ratio, L/B. For this geometry, the curvature can be calculated analytically (Section 2.4), and thus, the surface pressure can be obtained via Eq. (11). The first insert in Fig. 10 shows the drop at a modest deformation ($L/B = 1.2$), colored by surface pressure. The surface pressure is almost uniform with slightly higher values at the tips. The pressure difference between tip and waist drives a restoring flow stabilizing the drop (opposing deformation). As the deformation increases, the curvature increases at the tip whereas that at the waist decreases somewhat (compared to that of a sphere with the same volume) as illustrated by the inserts at $L/B = 2.0$ and 5.0. The tip-to-waist pressure difference (p_{tip}-p_{waist}) increases monotonically with deformation, indicating that the restoring internal flow continues to increase with increasing deformation. Consequently, a critical deformation such that observed for a droplet exposed to a turbulent flow (Fig. 4) is never reached for an ellipsoid.

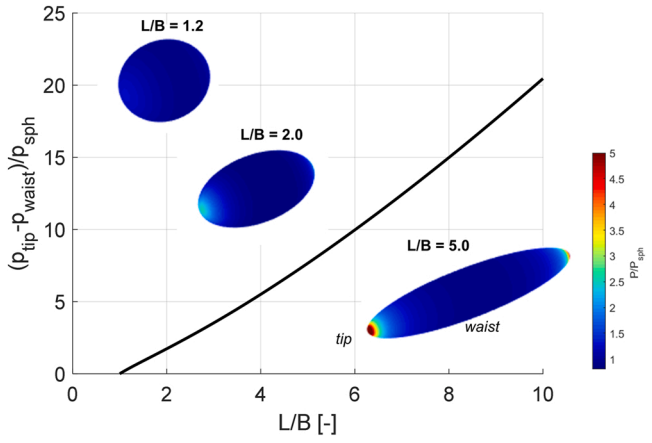

Fig. 10. Normalized static pressure difference between the tip and waist, p_{tip}-p_{waist}, of a prolate ellipsoid, as a function of its length-to-width ratio, L/B (assuming constant volume). The inserts show the normalized surface pressure, p/p_{sph}, for three different levels of deformation.

3.6. A simplistic criterion for identifying the critically deformed state

As argued in Section 3.4, a global static pressure maximum in the neck is a necessary and sufficient condition for reaching the critically deformed state. However, this criterion is difficult to apply in situations where the static pressure distribution is not known with great precision (e.g., in an in vitro high-speed breakup visualization study). If the 3D drop morphology was known with very high accuracy, it would (in principle) be possible to calculate the principal curvatures and use them to obtain the surface pressure (Eq. (11)). However, even if multiple cameras are used to reconstruct the 3D morphology of the drop [30,31], the algorithm used to estimate the local curvature would amplify even relatively small measurement uncertainties. An alternative is to introduce some simplifying assumptions and translate the maximum pressure criterion discussed in the previous section to something that is easier to quantify in an experimental setting. Such a simplistic model can be constructed inspired by the model for deformation time proposed by Xing et al. [44]:

Let us first assume that the drop deforms so that it forms two bulbs separated by a cylindrical filament or neck, see Fig. 11. The bulbs are approximately spherical (with radii $R_1 < R_2$), and the neck has a diameter D_{neck}. The critical state is reached when the static pressure in the neck exceeds that in the smallest bulb: $p_{neck} > p_1$, where the Laplace pressure in the smallest bulb is given by,

$$p_1 = p_0 + \frac{2\gamma}{R_1}. \tag{13}$$

For a cylinder, the first principal radius is equal to the cylinder radius, while the second principal radius is infinite, resulting in a pressure in the neck,

$$p_{neck} = p_0 + \frac{2\gamma}{D_{neck}}. \tag{14}$$

(Following, Xing et al. [44], Eqs. (13) and (14) assume that the pressure outside of the neck, p_0, is equal to that outside of the bulb, which is approximately true as seen in Fig. 7). Thus, the critical state is reached when,

$$p_{neck} = p_1 \quad => \quad D_{neck} = R_1. \tag{15}$$

Fig. 12 displays this relationship for the eight drops investigated in this study (solid markers), showing that the data fits the model surprisingly well given its simplistic nature: the critically deformed state is achieved approximately when the neck diameter equals the radius of the smallest bulb. The remaining seven flow initializations from Fig. 1 have also been inserted in Fig. 12 to further test the applicability of the proposed model. For these additional seven cases, the neck and bulb

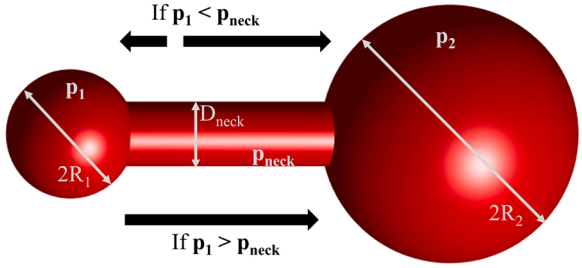

Fig. 11. Schematic illustration of the simplistic drop deformation model used to identify the critically deformed state.

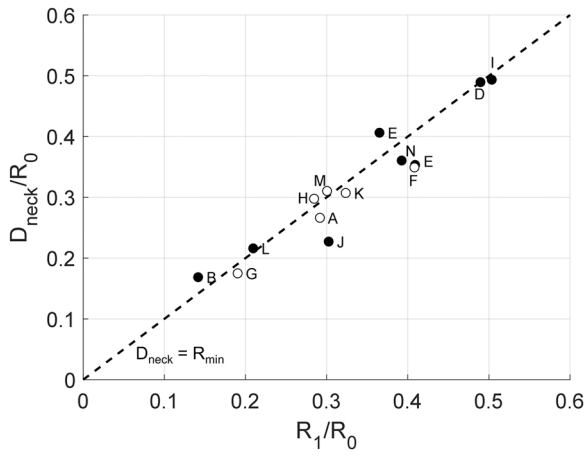

Fig. 12. Neck diameter at critical deformation, D_{neck}, versus the radius of the smallest bulb at critical deformation, R_1. Solid markers show data from the eight investigated drops (Fig. 3), whereas the dashed line shows the proposed model (see Eq. (15)). Open markers show data from the remaining seven drops from Fig. 1, where the critical state has been determined indirectly from the static pressure criterion.

diameters where obtained indirectly by first applying the static pressure criterion to identify the critical state (instead of determining the critical state independently through stability analysis as for the selected eight main cases). As seen in Fig. 12, both groups of flow initializations fit the proposed model.

Note that no assumptions are made about the value of the viscosity (or density) ratio and that the value of the interfacial tension does not appear in Eq. (15). Thus the criterion is expected to hold across a wide range of conditions for turbulent emulsion drop breakup. Also, note that the model can easily be extended to cases where the drop is deformed into more than two bulbs (e.g., drop F) by simply identifying R_1 with the radius of curvature of the smallest bulb (as seen in Fig. 12, drop F fits the model reasonably well with this extension). It should be noted, however, that the condition does not necessarily apply to foam bubble breakup where the internal flow is expected to be of substantially less importance due to the exceedingly low density and viscosity ratios.

3.7. *Effects of emulsifier dynamics*

One important limitation in the numerical deformation/stability analysis in general (and in the simplistic critical deformation criterion model in Section 3.6 in particular) is the assumption of a constant interfacial tension, both over time and along the interface. This assumption is typically made in numerical drop-breakup investigations [35–40] with notable exceptions [57]. However, it should be kept in mind that this need not apply under the experimental conditions of a single-drop high-speed breakup visualization study [9,27–33,58] or under industrially relevant turbulent emulsification e.g., in food, pharma and personal care emulsion processing. The magnitude of the local decrease of the interfacial tension is determined by the quantity of hydrophobic patches in contact with the interface, which, for a low-molecular weight emulsifier with high solubility in the aqueous phase, corresponds to the interface load of the molecules, Γ, (i.e., by the local interface concentration of the emulsifier). Domains with higher

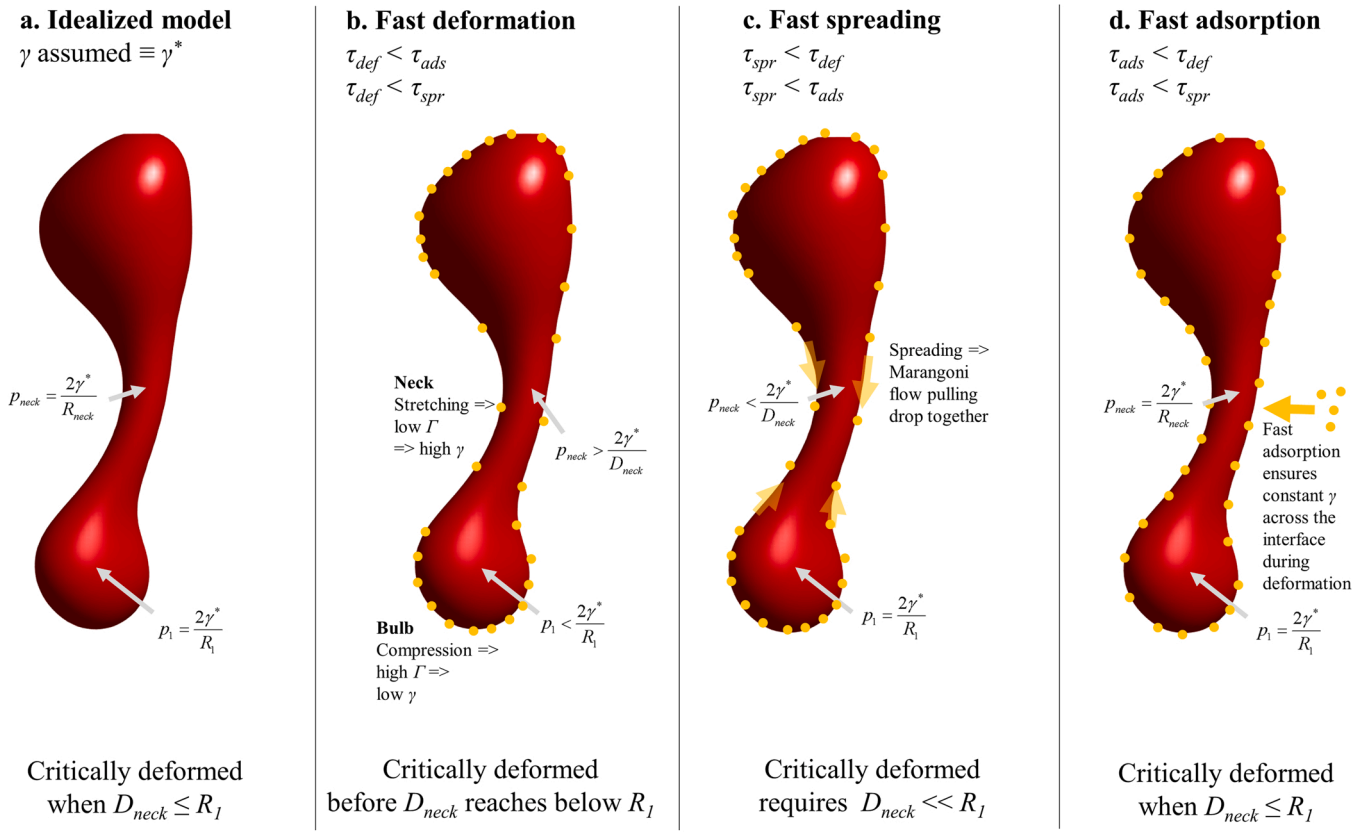

Fig. 13. Schematic representation of how the emulsifier dynamics is expected to influence the critical deformation criterion for four different 'regimes': (a) idealized conditions (γ constant), (b) fast deformation, (c) fast interface spreading of emulsifier and (d) fast adsorption of the emulsifier. The drop is depicted in red, whereas the emulsifier is schematically illustrated by yellow disks.

interface concentration of emulsifier have lower interfacial tension. The interface dynamics of the emulsifier has been described as a combination of deformation, adsorption and interface spreading [59,60]. Each process can be described by a characteristic time-scale: τ_{def} for deformation, τ_{ads} for adsorption and τ_{spr} for interface spreading. This theoretical framework can be used to gain some first insight into how the simplistic criterion in Section 3.6 needs to be further extended to account for less idealized systems (Fig. 13):

Drop deformation will compress the interface of the bulbs and stretch the interface at the neck (see Fig. 13a). If this deformation is fast enough, so that no significant amount of emulsifier is adsorbed from the continuous phase ($\tau_{def} < \tau_{ads}$), and fast enough so that the emulsifier does not have time to spread at the interface ($\tau_{def} < \tau_{spr}$), we will find an interface concentration gradient, inducing an interfacial tension gradient along the interface. This results in higher γ in the neck than on the bulbs (see Fig. 13b). If we let γ^* denote the average (steady-state) interfacial tension, then the neck pressure will be higher than in the ideal case (i.e., higher than in Fig. 13a), and the bulb pressure will be lower (due to γ differing between points at the surface). Consequently, under the assumption of fast deformation, the drop will reach a critically deformed state (i.e., it will reach $p_{neck} < p_1$) before D_{neck} has been deformed below R_1. In other words, it is easier to critically deform a drop (than indicated by Eq. (15)) if deformation is much faster than adsorption and interface spreading of the emulsifier.

The gradient in interface concentration created by the deformation will, however, induce an interface flux leading to a smoothening of emulsifier concentration along the interface. It has been argued that this process is dominated by longitudinal waves giving rise to interface spreading [60,61]. If we assume now that this process is fast in relation to both the deformation and to the adsorption of new emulsifier to the interface ($\tau_{spr} < \tau_{def}$ and $\tau_{spr} < \tau_{ads}$), see Fig. 13c, there will be no effective gradients in interfacial load and interfacial tension. However, the interface flux of emulsifier, flowing from the compressed bulbs (high interfacial load) to the stretched neck (low interfacial load), will give rise to a Marangoni flow, pulling with it the fluid inside of the drop. This flow is restoring, adding to the Laplace pressure-induced flow that acts to contract the drop under sub-critical conditions. Thus, under conditions where the emulsifier spreading is the fastest process, the neck will need to be more heavily deformed (than indicated by Eq. (15)) in order to reach a critically deformed state.

Lastly, we consider a case where the adsorption is substantially faster than both deformation and interface spreading ($\tau_{ads} < \tau_{def}$ and $\tau_{ads} < \tau_{spr}$), Fig. 13d. If new emulsifier is continuously adsorbing to (and desorbing from) the interface, then the interfacial tension will effectively be constant over the interface and over time (assuming that the molecular exchange between the adsorbed and desorbed state is rapid). Thus, under conditions of fast adsorption, the interface will behave as specified in the idealized model (uniform interfacial tension), and the critical state is expected to occur when $D_{neck} = R_1$.

From Fig. 13 and the discussion above, we see that the extent to which Eq. (15) is directly applicable for identifying a critically deformed state under non-ideal conditions, depends on the relation between time scales. Attempts have been made to approximate these time scales for different emulsification devices and emulsifier systems [60–65]. However, there is still no general agreement on the relationship between these time-scales. A further complication is the difficulty in knowing which interfacial tension should be used in the expressions proposed to estimate these time scales. As comprehensively discussed by Shroën et al. [64] the interfacial tension relevant during deformation/breakup is the dynamic one, acting over milliseconds or microseconds, whereas most measurement techniques provide the steady-state value or only describe the dynamics which are several orders of magnitude slower.

In summary, the static pressure criterion ($p_{neck} \geq p_1$) is a general property of the critically deformed state. However, the geometric criterion ($D_{neck} \leq R_1$) is only expected to apply in its exact form in situations where emulsifier adsorption is substantially faster than deformation and interface spreading.

4. Conclusions

Numerical breakup experiments have been used to characterize when a viscous drop undergoing turbulent breakup has reached a critically deformed state, i.e., a state after which it will eventually and deterministically break.

The critically deformed state is characterized by the formation of a neck separating two (or occasionally more) bulbs. The neck has a highly negative Gaussian curvature in a collection of points, indicative of saddle points. The total interfacial area is a poor indicator of when the critically deformed state has been reached.

The critically deformed state occurs when the neck has been sufficiently deformed to have a curvature that exceeds that of the smallest bulb. This implies that the static pressure is higher in the neck than in both bulbs and, consequently, the flow inside the droplet is from the neck into both bulbs, further thinning the neck until rupture. This destabilizing flow can be compared to the situation in pre-critical states, where the global maximum of the static pressure is found in the smallest bulb, which gives rise to a stabilizing internal flow, pushing fluid back into the larger bulb.

A simplistic model (assuming the drop deforms into two bulbs separated by a cylindrical neck) is suggested to translate this breakup criterion based on static pressure into a criterion that can be applied in an experimental setting directly examining the droplet geometry. The model indicates that critical deformation is reached when the neck diameter is smaller than the radius of the smallest bulb. This simplistic model fits the numerical data fairly well, indicating that the proposed criterion can be a useful method for finding the critical point in time or space where the drop critical deformation occurs. We finally argue that this geometrical criterion is valid when interfacial tension is assumed constant or adsorption of new emulsifier to the deforming interface is sufficiently fast, while it could be improved to account for a non-uniform emulsifier concentration in the case of fast deformation and fast spreading of emulsifier at the interface. In the first case, we expect a more stringent criterion for critical deformation, while fast spreading may decrease the time necessary for reaching a critically deformed state.

CRediT authorship contribution statement

Andreas Håkansson: Conceptualization, Investigation, Formal analysis, Writing – original draft, Funding acquisition. **Marco Crialesi-Esposito**: Methodology, Software, Validation, Writing – review & editing. **Lars Nilsson**: Conceptualization, Writing – review & editing. **Luca Brandt**: Methodology, Software, Resources, Writing – review & editing.

Declaration of Competing Interest

The authors declare that they have no known competing financial interests or personal relationships that could have appeared to influence the work reported in this paper.

Acknowledgments

Prof. Fredrik Innings and Peyman Olad are gratefully acknowledged for valuable discussions on the nature of turbulent drop breakup and homogenization. This research was funded by The Swedish Research Council (VR), Grant number 2018-03820, and Tetra Pak Processing Systems AB.

References

[1] S.N. Kale, S.L. Deore, Emulsion micro emulsion and nano emulsion: a review, Syst. Rev. Pharm. 8 (1) (2017) 39–47, https://doi.org/10.5530/srp.2017.1.8.

[2] D.J. McClements, Food Emulsions: Principles, Practices, and Techniques, CRC Press, Boca Raton, 2016.

[3] T.F. Tadros, Emulsion Formation and Stability, Wiley-VCH, Weinheim, 2013.

[4] J.J.M. Janssen, H. Hoogland, Modelling strategies for emulsification in industrial practice, Can. J. Chem. Eng. 92 (2014) 198–202, https://doi.org/10.1002/cjce.21942.

[5] H. Steiner, R. Teppner, G. Brenn, N. Vankova, S. Tcholakova, N. Denkov, Numerical simulation and experimental study of emulsification in a narrow-gap homogenizer, Chem. Eng. Sci. 61 (2006) 5841–5855, https://doi.org/10.1016/j.ces.2006.04.016.

[6] M. Ashar, D. Arlov, F. Carlsson, F. Innings, R. Andersson, Single droplet breakup in a rotor-stator mixer, Chem. Eng. Sci. 181 (2018) 186–198, https://doi.org/10.1016/j.ces.2018.02.021.

[7] A. Håkansson, An experimental investigation of the probability distribution of turbulent fragmenting stresses in a high-pressure homogenizer, Chem. Eng. Sci. 177 (2018) 139–150, https://doi.org/10.1016/j.ces.2017.11.045.

[8] F. Innings, C. Trägårdh, Visualization of the drop deformation and break-up process in a high-pressure homogenizer, Chem. Eng. Technol. 28 (2005) 882–891, https://doi.org/10.1002/ceat.200500080.

[9] K. Kelemen, S. Gepperth, R. Koch, H.J. Bauer, H.P. Schuchmann, On the visualization of droplet deformation and breakup during high-pressure homogenization, Microfluid. Nanofluid. 19 (2015) 1139–1158, https://doi.org/10.1007/s10404-015-1631-z.

[10] B. Mutsch, F.J. Preiss, T. Dagenbach, H.P. Karbstein, C.J. Kähler, Scaling of droplet breakup in high-pressure homogenizer orifices. Part II: visualization of the turbulent droplet breakup, ChemEngineering 5 (2021), e5010007, https://doi.org/10.3390/chemengineering5010007.

[11] F.J. Preiss, B. Mutsch, C.J. Kähler, H.P. Karbstein, Scaling of droplet breakup in high-pressure homogenizer orifices. Part I: comparison of velocity profiles in scaled coaxial orifices, ChemEngineering 5 (2021), e5010007, https://doi.org/10.3390/chemengineering5010007.

[12] J.O. Hinze, Fundamentals of the hydrodynamic mechanism of splitting in dispersion process, AIChE J. 1 (1955) 289–295, https://doi.org/10.1002/aic.690010303.

[13] A.N. Kolmogorov, On the breakage of drops in a turbulent flow. Dokl. Akad. Nauk. SSSR. 1949; 66: 825–828. (Originally in Russian. Reprinted and translated in Selected Works of A.N. Kolmogorov, Volume 1: Mathematics and Mechanics, Tikhomirov, V.M. (ed.), 1991, pp. 339–343).

[14] R. Shinnar, On the behaviour of liquid dispersions in mixing vessels, J. Fluid Mech. 10 (2) (1961) 259–275, https://doi.org/10.1017/S0022112061000214.

[15] K. Arai, M. Konno, Y. Mutunaga, S. Saito, Effect of dispersed-phase viscosity on the maximum stable drop size for breakup in turbulent flow, J. Chem. Eng. Jpn. 10 (1977) 325–330, https://doi.org/10.1252/JCEJ.10.325.

[16] R.V. Calabrese, T.P.K. Chang, P.T. Dang, Drop breakup in turbulent stirred-tank contactors. Part I: effect of dispersed-phase viscosity, AIChE J. 32 (4) (1986) 657–666, https://doi.org/10.1002/aic.690320416.

[17] J.T. Davies, Drop sizes of emulsions related to turbulent energy dissipation rates, Chem. Eng. Sci. 40 (1985) 839–842, https://doi.org/10.1016/0009-2509(85)85036-3.

[18] J. Bałdyga, W. Podgorska, Drop break-up in intermittent turbulence: maximum stable and transient sizes of drops, Can. J. Chem. Eng. 76 (1998) 456–470, https://doi.org/10.1002/cjce.5450760316.

[19] A. Håkansson, The role of stochastic time-variations in turbulent stresses when predicting drop breakup – a review of modelling approaches, Processes 9 (2021) 1904, https://doi.org/10.3390/pr9111904.

[20] N. Vankova, S. Tcholakova, N.D. Denkov, I. Ivanov, V.D. Vulchev, T. Danner, Emulsification in turbulent flow 1. Mean and maximum drop diameters in inertial and viscous regimes, J. Colloid Interface Sci. 312 (2007) 363–380, https://doi.org/10.1016/j.jcis.2007.03.059.

[21] A.K. Aiyer, D. Yang, M. Chamecki, C. Meneveau, A population balance model for large eddy simulation of polydisperse droplet evolution, J. Fluid Mech. 878 (2019) 700–739, https://doi.org/10.1017/jfm.2019.649.

[22] A. Håkansson, Experimental methods for measuring the breakup frequency in turbulent emulsification: a critical review, ChemEngineering 4 (2020) 52, https://doi.org/10.3390/chemengineering4030052.

[23] Y. Liao, D. Lucas, A literature review of theoretical models for drop and bubble breakup in turbulent dispersions, Chem. Eng. Sci. 64 (2009) 3389–3406, https://doi.org/10.1016/j.ces.2009.04.026.

[24] S.N. Maindarkar, H. Hoogland, M.A. Hansen, Predicting the combined effects of oil and surfactant concentrations on the drop size distributions of homogenized emulsions, Colloids Surf. A Physicochem. Eng. Asp. 467 (2015) 18–30, https://doi.org/10.1016/j.colsurfa.2014.11.032.

[25] N.B. Raikar, S.R. Bhatia, M.F. Malone, D.J. McClements, M.A. Henson, Predicting the effect of the homogenization pressure on emulsion drop-size distributions, Ind. Eng. Chem. Res. 50 (2011) 6089–6100, https://doi.org/10.1021/ie101818h.

[26] J. Solsvik, S. Tangen, H.A. Jakobsen, On the constitutive equations for fluid particle breakage, Rev. Chem. Eng. 29 (5) (2013) 241–356, https://doi.org/10.1515/revce-2013-0009.

[27] E.H. Herø, N. La Forgia, J. Solsvik, H.A. Jakobsen, Single drop breakage in turbulent flow: statistical data analysis, Chem. Eng. Sci. X 8 (2020), e100082, https://doi.org/10.1016/j.cesx.2020.100082.

[28] N. La Forgia, E.H. Herø, H.A. Jakobsen, High-speed image processing of fluid particle breakage in turbulent flow, Chem. Eng. X 12 (2021), e100117, https://doi.org/10.1016/j.cesx.2021.100117.

[29] S. Maaß, M. Kraume, Determination of breakage rates using single drop experiments, Chem. Eng. Sci. 70 (2012) 146–164, https://doi.org/10.1016/j.ces.2011.08.027.

[30] A.U.M. Masuk, A.K.R. Salibindla, R. Ni, Simultaneous measurements of deforming Hinze-scale bubbles with surrounding turbulence, J. Fluid Mech. 910 (2021) A21, https://doi.org/10.1017/jfm.2020.933.

[31] Y. Qi, S. Tan, N. Corbitt, C. Urbanik, A.K.R. Salibindla, R. Ni, Fragmentation in turbulence by small eddies, Nat. Commun. 13 (2022) 469, https://doi.org/10.1038/s41467-022-28092-3.

[32] J. Solsvik, S. Maaß, H.A. Jakobsen, Definition of the single drop breakup event, Ind. Eng. Chem. Res. 55 (10) (2016) 2872–2882, https://doi.org/10.1021/acs.iecr.6b00591.

[33] J. Solsvik, H.A. Jakobsen, Single drop breakup experiments in stirred liquid-liquid tank, Chem. Eng. Sci. 131 (2015) 219–234, https://doi.org/10.1016/j.ces.2015.03.059.

[34] A. Håkansson, L. Brandt, Deformation and initial breakup morphology of viscous emulsion drops in isotropic homogeneous turbulence with relevance for emulsification devices, Chem. Eng. Sci. (2022), https://doi.org/10.1016/j.ces.2022.117599 (In press).

[35] M. Karimi, R. Andersson, Stochastic simulation of droplet breakup in turbulence, Chem. Eng. J. 380 (2020), 122502, https://doi.org/10.1016/j.cej.2019.122502.

[36] A.E. Komrakova, Single drop breakup in turbulent flow, Can. J. Chem. Eng. 97 (2019) 2727–2739, https://doi.org/10.1002/cjce.23478.

[37] D. Qian, J.B. McLaughlin, K. Sankaranarayanan, S. Sundaresan, K. Kontomaris, Simulation of bubble breakup dynamics in homogenous turbulence, Chem. Eng. Commun. 193 (2006) 1038–1063, https://doi.org/10.1080/00986440500354275.

[38] A. Rivière, W. Mostert, S. Perrard, L. Deike, Sub-Hinze scale bubble production in turbulent bubble break-up, J. Fluid Mech. 917 (2021) A40, https://doi.org/10.1017/jfm.2021.243.

[39] M.E. Rosti, F. De Vita, L. Brandt, Numerical simulations of emulsions in shear flows, Acta Mech. 230 (2) (2019) 667–682, https://doi.org/10.1007/s00707-018-2265-5.

[40] C. Shao, K. Luo, Y. Yang, J. Fan, Direct numerical simulation of droplet breakup in homogeneous isotropic turbulence: the effect of the Weber number, Int. J. Multiph. Flow 107 (2018) 263–274, https://doi.org/10.1016/j.ijmultiphaseflow.2018.06.009.

[41] L. Brandt, F. Coletti, Particle-laden turbulence: progress and perspectives, Annu. Rev. Fluid Mech. 54 (2022) 159–189, https://doi.org/10.1146/annurev-fluid-030121-021103.

[42] S. Elghobashi, Direct numerical simulation of turbulent flows laden with droplets or bubbles, Annu. Rev. Fluid Mech. 51 (2019) 217–244, https://doi.org/10.1146/annurev-fluid-010518-040401.

[43] P. Perlekar, L. Biferale, M. Sbragaglia, S. Srivastava, F. Toschi, Droplet size distribution in homogeneous isotropic turbulence, Phys. Fluids 24 (2012), 065101, https://doi.org/10.1063/1.4719144.

[44] C. Xing, T. Wang, K. Guo, J. Wang, A unified theoretical model for breakup of bubbles and droplets in turbulent flows, AIChE J. 61 (2015) 1391–1403, https://doi.org/10.1002/aic.14709.

[45] A. Vela-Martín, M. Avila, Deformation of drops by outer eddies in turbulence, J. Fluid Mech. 929 (2021) A38, https://doi.org/10.1017/jfm.2021.879.

[46] R. Andersson, A. Helmi, Computational fluid dynamics simulation of fluid particle fragmentation in turbulent flows, Appl. Math. Model. 38 (17–18) (2014) 4186–4196, https://doi.org/10.1016/j.apm.2014.01.005.

[47] C. Planchette, F. Marangon, W.-K. Hsiao, G. Brenn, Breakup of asymmetric liquid ligaments, Phys. Rev. Fluids 4 (2019), 124004, https://doi.org/10.1103/PhysRevFluids.4.124004.

[48] S. Ii, B. Xie, F. Xiao, An interface capturing method with a continuous function: the THINC method on unstructured triangular and tetrahedral meshes, J. Comput. Phys. 259 (2014) 260–269, https://doi.org/10.1016/j.jcp.2013.11.034.

[49] P. Costa, A FFT-based finite-difference solver for massively-parallel direct numerical simulations of turbulent flows, Comput. Math. Appl. 76 (8) (2018) 1853–1862, arXiv:1802.10323v3.

[50] M. Crialesi-Esposito, M.E. Rosti, S. Chibbaro, L. Brandt, Modulation of homogeneous and isotropic turbulence in emulsions, J. Fluid Mech. 490 (2022) A19, https://doi.org/10.1017/jfm.2022.179.

[51] V. Eswaran, S.B. Pope, An examination of forcing in direct numerical simulations of turbulence, Comput. Fluids 16 (1988) 257–278, https://doi.org/10.1016/0045-7930(88)90013-8.

[52] L.F. Shampine, Vectorized adaptive quadrature in MATLAB, J. Comput. Appl. Math. 211 (2008) 131–140, https://doi.org/10.1016/j.cam.2006.11.02.

[53] N. Dyn, K. Hormann, S.J. Kim, D. Levin, Optimizing 3D triangulations using discrete curvature analysis, in: T. Lyche, L.L. Schumaker (Eds.), Mathematical Methods for Curves and Surfaces, Vanderbilt University Press, Nashville, 2001, pp. 135–146.

[54] U. Ayachit, The ParaView Guide: A Parallel Visualization Application, Kitware, New-York, 2015.

[55] E. Albin, R. Knikker, S. Xin, C.O. Paschereit, Y.D. D'Angelo, Computational assessment of curvatures and principal directions of implicit surfaces from 3D scalar data, in: M. Floater, T. Lyche, M.L. Mazure, K. Mørken, L. Schumaker (Eds.), Mathematical Methods for Curves and Surfaces. MMCS 2016. Lecture Notes in Computer Science Vol. 10521, Springer, New-York, 2017, pp. 1–22, https://doi.org/10.1007/978-3-319-67885-6_1.

[56] E. Abbena, S. Salamon, A. Gray. Modern Differential Geometry of Curves and Surfaces with Mathematica, 2nd ed., CRC Press, Boca Raton, 1997, pp. 301–303.
[57] R. Skartlien, E. Sollum, H. Schumann, Droplet size distributions in turbulent emulsions: breakup criteria and surfactant effects from direct numerical simulations, J. Chem. Phys. 139 (2013), 174901, https://doi.org/10.1063/1.4827025.
[58] J. Vejražka, M. Zedníková, P. Stranovský, Experiments on breakup of bubbles in a turbulent flow, AIChE J. 64 (2018) 740–757, https://doi.org/10.1002/aic.15935.
[59] V. Levich, Physicochemical Hydrodynamics, Prentice Hall, Eaglewood Cliffs, 1962.
[60] P. Walstra, Emulsions, in: J. Lyklema (Ed.), Fundamentals of Interface and Colloid Science, Elsevier, Amsterdam, 2005.
[61] P. Walstra, I. Smulders, Emulsion formation, in: B.P. Binks (Ed.), Modern Aspects of Emulsion Science, The Royal Society of Chemistry, Cambridge, 1998, pp. 56–99.
[62] L. Nilsson, M. Leeman, K.-G. Wahlund, B. Bergenståhl, Competitive adsorption of a polydisperse polymer during emulsification: experiments and modeling, Langmuir 23 (2007) 2346–2351, https://doi.org/10.1021/la062483b.
[63] M. Rayner, Scales and forces in emulsification, in: M. Rayner, P. Dejmek (Eds.), Engineering Aspects of Food Emulsification and Homogenization, CRC Press, Boca Raton, 2015, pp. 3–32.
[64] K. Shroën, J. de Ruiter, C. Berton-Carabin, The importance of interfacial tension in emulsification: connecting scaling relations used in large scale preparation with microfluidic measurement methods, ChemEngineering 4 (2020) 63, https://doi.org/10.3390/chemengineering4040063.
[65] S. Tcholakova, N. Denkov, T. Danner, Role of surfactant type and concentration for the mean drop size during emulsification in turbulent flow, Langmuir 20 (2004) 7444–7458, https://doi.org/10.1021/la049335a.